



ELSEVIER

Contents lists available at ScienceDirect

Diamond & Related Materials

journal homepage: www.elsevier.com/locate/diamond

Modeling current transport in boron-doped diamond at high electric fields including self-heating effect

N. Lambert^{a,b,*}, A. Taylor^a, P. Hubík^a, J. Bulíř^a, J. More-Chevalier^a, H. Karaca^c, C. Fleury^{c,d}, J. Voves^b, Z. Šobán^a, D. Pogany^c, V. Mortet^{a,e}

^a FZU - Institute of Physics of the Czech Academy of Sciences, Na Slovance 1999/2, 182 21 Prague 8, Czech Republic

^b Faculty of Electrical Engineering, Czech Technical University in Prague, Technická 1902/2, 166 27 Prague, Czech Republic

^c Institute of Solid State Electronics, Technische Universität Wien, Gusshausstraße 25, 1040 Vienna, Austria

^d Silicon Austria Labs, Europastraße 12, 9524 Villach, Austria

^e Faculty of Biomedical Engineering, Czech Technical University in Prague, Sítna 3105, 272 01 Kladno, Czech Republic

ARTICLE INFO

Keywords:

Boron-doped diamond

Pulsed measurement

Impurity impact ionization

Self-heating

High electric field measurement

Thermal simulation

ABSTRACT

In this work, current multiplication at high electric field in epitaxial boron-doped diamond with high acceptor concentration is analyzed, including self-heating effect and impurity impact ionization. Quasi-static current-voltage (I-V) characteristics were measured using a transmission-line pulse setup with 100 ns pulse duration on samples with two Ohmic titanium/gold electrodes. Unambiguous exponential and super-exponential behaviors are observed in the I-V curves along with, in some cases, negative differential resistance. The self-heating effect is analyzed using transient interferometric mapping of the thermal energy distribution between electrodes with a ns time scale. Measured I-V characteristics are modeled by finite element method and by considering boron acceptor ionization due to self-heating effect and impurity impact ionization. Simulated I-V characteristics, in particular the appearance of the negative differential resistance region attributed to self-heating, are in good agreement with experimental data.

1. Introduction

Diamond is a semiconductor with intrinsic properties particularly promising for power electronics with high thermal conductivity, high carrier mobility and high breakdown field [1]. The development of diamond-based electronic devices is currently supported by steady progress in n-type [2] and p-type [3] doping and hetero-epitaxial [4] diamond growth. These achievements have enabled demonstration of various diodes [5–7] and transistors [8,9]. Knowledge of diamond electrical properties in high electric fields is crucial in the design and fabrication of power electronic devices. Contrary to other low band gap semiconductors, used in microelectronics, only a small part of dopants (boron or phosphorus) is ionized at room temperature in diamond [10]. Recent experimental studies at high electric fields of boron-doped diamond reported a rapid current multiplication above a threshold voltage, which is a function of the inter-electrode gap, the boron concentration and the temperature [11,12]. This phenomenon has been attributed to Impurity Impact Ionization (III), a freeze-out regime effect, which has been also reported for germanium and silicon carbide [13,14].

In this article, we analyze by finite element simulation the experimental transient voltage/current response and related quasi-static I-V characteristics of boron-doped diamond devices. We discuss different mechanisms to interpret the observed exponential I-V characteristic and Negative Differential Resistance (NDR) regime: Poole-Frenkel Effect (PFE) [15], Phonon-Assisted Tunneling Effect (PATE) [16], III, and Self-Heating Effect (SHE), and we discuss their role regarding the observed current multiplication.

2. Experimental setup

Epitaxial boron-doped diamond (100) layers were grown by microwave plasma enhanced chemical vapor deposition using a commercial ASTeX 5010 reactor (Seki Technotron, Japan) in a hydrogen plasma with a minute addition of methane and trimethylborane [12]. The boron concentration [B] of the layers, which ranges from $3.2 \times 10^{18} \text{ cm}^{-3}$ to $6.3 \times 10^{19} \text{ cm}^{-3}$ (details are given in Table 1), was calculated from the incorporation ratio determined from Secondary Ion Mass Spectroscopy (SIMS) measurements of boron-doped diamonds samples from reference [12]. The error on the calculated boron

* Corresponding author at: FZU - Institute of Physics of the Czech Academy of Sciences, Na Slovance 1999/2, 182 21 Prague 8, Czech Republic.

E-mail address: lambert@fzu.cz (N. Lambert).

<https://doi.org/10.1016/j.diamond.2020.108003>

Received 23 April 2020; Received in revised form 3 July 2020; Accepted 7 July 2020

Available online 22 July 2020

0925-9635/ © 2020 Elsevier B.V. All rights reserved.

Table 1
Physical characteristics of diamond samples and simulation parameters used in the finite element method simulation.

		Sample A	Sample B	Sample C	Sample D
Physical characteristics					
	Geometry of electrodes	Circular	Circular	Circular	Parallel
	Inter-electrode gap (μm)	16.6	12.8	14.8	14.3
	Doped diamond layer thickness (μm)	3.36	5.50	3.27	1.36
	Boron concentration (estimated from SIMS data in reference [12]) (cm^{-3})	3.2×10^{18}	3.8×10^{19}	6.3×10^{19}	3.6×10^{19}
	Breakdown voltage (V)	110	125	215	255
Simulation parameters					
PATE	Carrier lifetime [20] (s)		1.2×10^{-11}		
	Carrier capture cross section [21] (cm^{-2})		10^{-14}		
SHE & III	Donor concentration (cm^{-3})	4.8×10^{16}	1.9×10^{18}	4.1×10^{18}	3.0×10^{18}
	A_{α} (cm^{-1})	1.4×10^3	1.2×10^3	1.0×10^3	1.2×10^3
	B_{α} ($\text{V}\cdot\text{cm}^{-1}$)	8.4×10^4	4.6×10^4	6.2×10^4	4.6×10^4
	A_{cv} ($\text{J}\cdot\text{cm}^{-3}\cdot\text{K}^{-1}$)			4.0×10^{-1}	
	B_{cv} ($\text{J}\cdot\text{cm}^{-3}\cdot\text{K}^{-2}$)			1.1×10^{-2}	
	C_{cv} ($\text{J}\cdot\text{cm}^{-3}\cdot\text{K}^{-3}$)			-4.0×10^{-6}	
	D_{cv} ($\text{J}\cdot\text{K}\cdot\text{cm}^{-3}$)			-1.1×10^5	
	v_{sat} ($\text{cm}\cdot\text{s}^{-1}$)			1.1×10^7	
	β_{sat}			9.5×10^{-1}	

concentration is about $2 \times 10^{18} \text{ cm}^{-3}$. Transient response and quasi-static current-voltage (I-V) characteristics were measured using a 100 ns transmission-line pulse setup [9] on concentric ring-and-disk electrodes test structures with an inner disk electrode diameter of 150 μm and an inter-electrode gap of around 15 μm . The ring-disk concentric electrodes have Ohmic contacts consisting of a titanium (10 nm) and gold (200 nm) bilayer deposited by e-beam evaporation in an Edwards Auto 500 vacuum coater and annealed at 450 $^{\circ}\text{C}$ for 20 min [17]. The electrodes were patterned by photolithography and wet chemical etching of the titanium and gold bilayer. The transient heat energy distribution between the electrodes was measured by Transient Interferometric Mapping (TIM) method [18]. The temperature-variation in the boron-doped diamond layer was measured via the change in the diamond refractive index, which results in a change in phase shift of a probing laser beam [19]. The probing beam goes through the sample from the backside, reflects on the top surface, and returns to the microscope objective. The optical phase shift, which is detected interferometrically, is proportional to the heat energy density in the sample [18]. The samples are stressed by 100 ns long voltage pulses at a 1 Hz repetition frequency (assuring cooling to room temperature before the next pulse) while transient phase shift is recorded. The phase distribution is determined point-by-point by moving the beam position. As the system does not allow measurements on test structures with circular geometries, TIM measurements were carried out on 75 μm wide parallel titanium/gold electrodes with a 14.3 μm inter-electrode gap patterned (Table 1).

3. Experimental results

Fig. 1 shows typical characteristic voltage and current waveforms of boron-doped diamond sample B ($[B] = 3.8 \times 10^{19} \text{ cm}^{-3}$) during voltage pulses with different charging voltages V_{ch} . At applied voltages lower than 100 V, the voltage and current waveforms are nearly flat during the 100 ns pulse, which indicates that there is no significant heating and temperature variation in the device. At larger applied voltages, both the voltage and current vary in time, which is characteristic of thermal runaway due to SHE and the current intensity further increases with the increasing V_{ch} until catastrophic breakdown. This phenomenon is also visible in Fig. 1c in which I-V curves have been plotted for four different averaging periods during the voltage pulse. For a voltage lower than 100 V, the I-V curves are very similar while a divergence is observed for a voltage higher than 100 V. The later the averaging is done during the pulse, the higher the resulting current is. A NDR region in the I-V curve also emerges for longer times at currents above 1 A. The spike at the beginning of the current pulse (observed in

Fig. 1b) is an artefact due to the propagation of the signal in the cable between the probe and the sample.

Fig. 2 shows quasi-static I-V characteristics for all samples in linear (a) and semi-logarithmic (b) scale determined from waveforms with different V_{ch} (cf. also Fig. 1). The average value of voltage and current were calculated at the end of each pulse, i.e. between 85 ns and 95 ns from the beginning of each pulse. Each curve exhibits a short linear part up to approximately 50 V which transitions to an exponential behavior as the voltage increases. Finally, the current increases even further with a super-exponential evolution until the breakdown voltage (V_{bd}) indicated by dashed lines in Fig. 2 and reported in Table 1. Sample B shows a NDR region at currents above 1.0 A, i.e. for V_{ch} superior to 150 V, cf. also Fig. 1c. The instantaneous voltage decreases rapidly while the instantaneous current increases (Fig. 1), causing the NDR.

Besides the III effect, the origin of the non-linear increase in current, especially the NDR regime, and the following breakdown observed in I-V characteristics could be attributed to SHE. Therefore, TIM measurements were carried-out on boron-doped diamond layers with parallel electrodes to investigate the possible self-heating effect. Thermal energy distribution maps were obtained through multiple pulsed measurements. Since repeated pulses in the NDR regime gradually degrade the electrodes, TIM measurements were performed below and at the onset of the NDR region.

Fig. 3a shows the phase shift distribution in the inter-electrode gap space of sample D below the NDR regime's onset, i.e. at a constant (final) current 50 mA in the exponential region. This condition is indicated by the left arrow in the I-V curve of sample D in Fig. 2. The phase shift increases non-linearly with time until the end of the pulse ($t = 100 \text{ ns}$), where it is at maximum (0.05 rad) and then decreases. The uniform phase shift along the device's electrodes width (X-direction) demonstrates a uniform current distribution.

Fig. 3b shows TIM measurement made at the onset of the NDR, i.e. at a current of 250 mA (see the right arrow label in the I-V curve of sample D in Fig. 2). While the phase shift at $t = 50 \text{ ns}$ is still homogeneous along the X-axis, it becomes non-uniform at longer times and forms two peaks at the end of the pulse with a maximum value of approximately 0.24 rad. The two peaks are attributed to the formation of two hot spots between the electrodes due to current filamentation and thermal runaway [22].

Fig. 3c represents the measured phase shift between the electrodes along the electric current path, i.e. perpendicularly to the electrodes, for the current of 0.25 A and positive polarity on the right electrode. The heat distribution peaks in the region between the electrodes. The phase shift distribution is nearly identical for the opposite polarity between the electrodes. The sharp negative peaks of the phase shift at

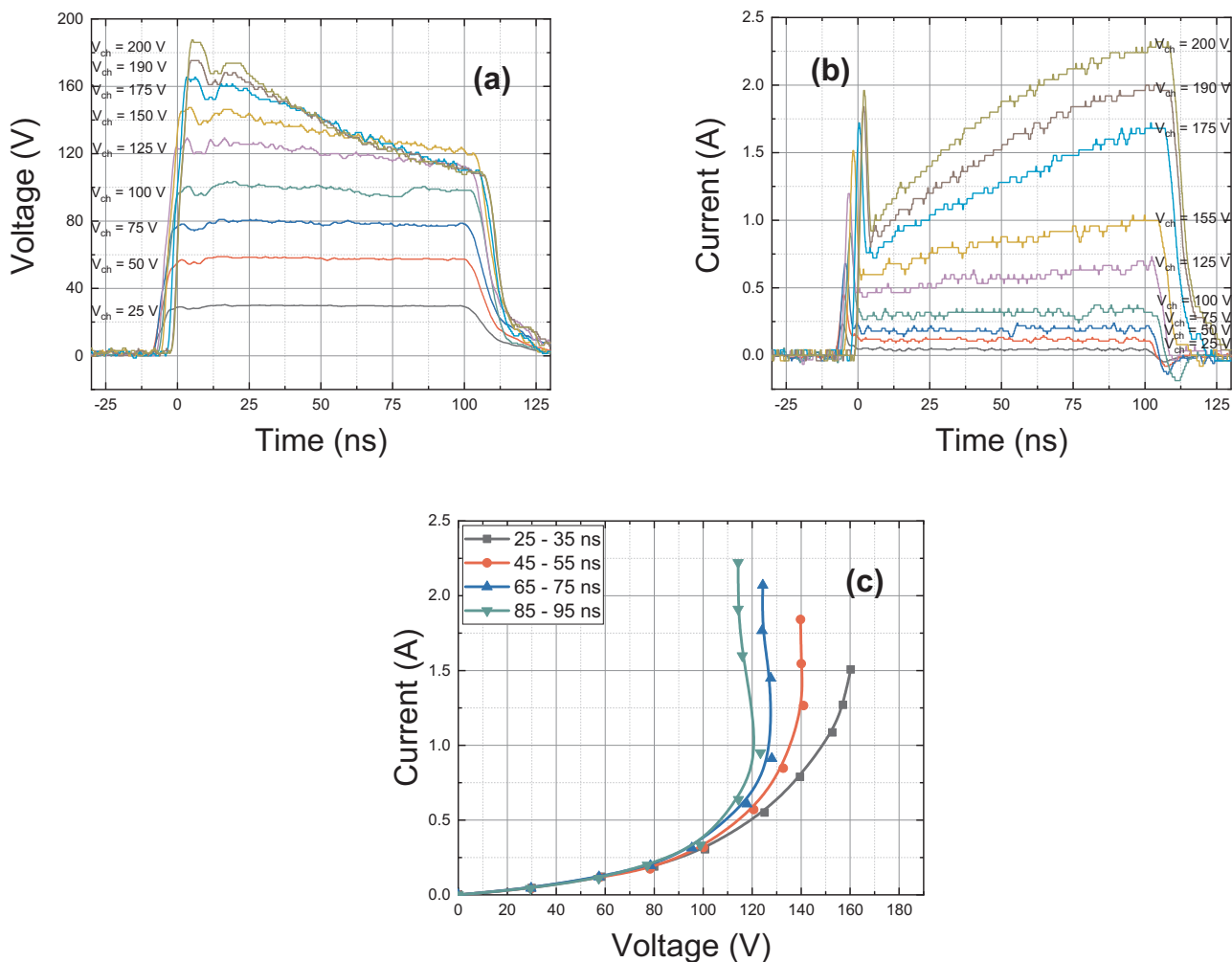


Fig. 1. Measured (a) voltage and (b) current waveform of sample B ($[B] = 3.8 \times 10^{19} \text{ cm}^{-3}$) for different charging voltage V_{ch} , and I-V characteristics (c) calculated for different averaging periods in the voltage (a) and current (b) waveforms. The initial peak of current in (b) and small voltage steps in (a) are artefacts due to different spatial position of voltage and current probes and reflections. The lines in (c) are for eye-guiding.

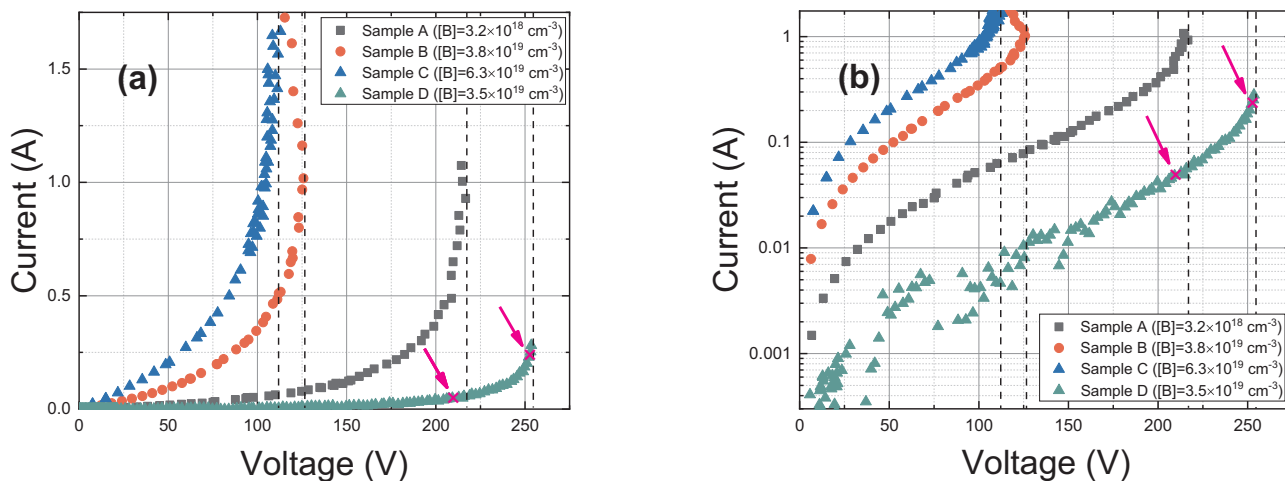


Fig. 2. Current-voltage characteristic of studied devices in linear and semi-logarithmic (b) scales. In sample D, two measurement conditions (50 mA and 250 mA) at which TIM measurements were performed are indicated by pink arrows and crosses. (For interpretation of the references to colour in this figure legend, the reader is referred to the web version of this article.)

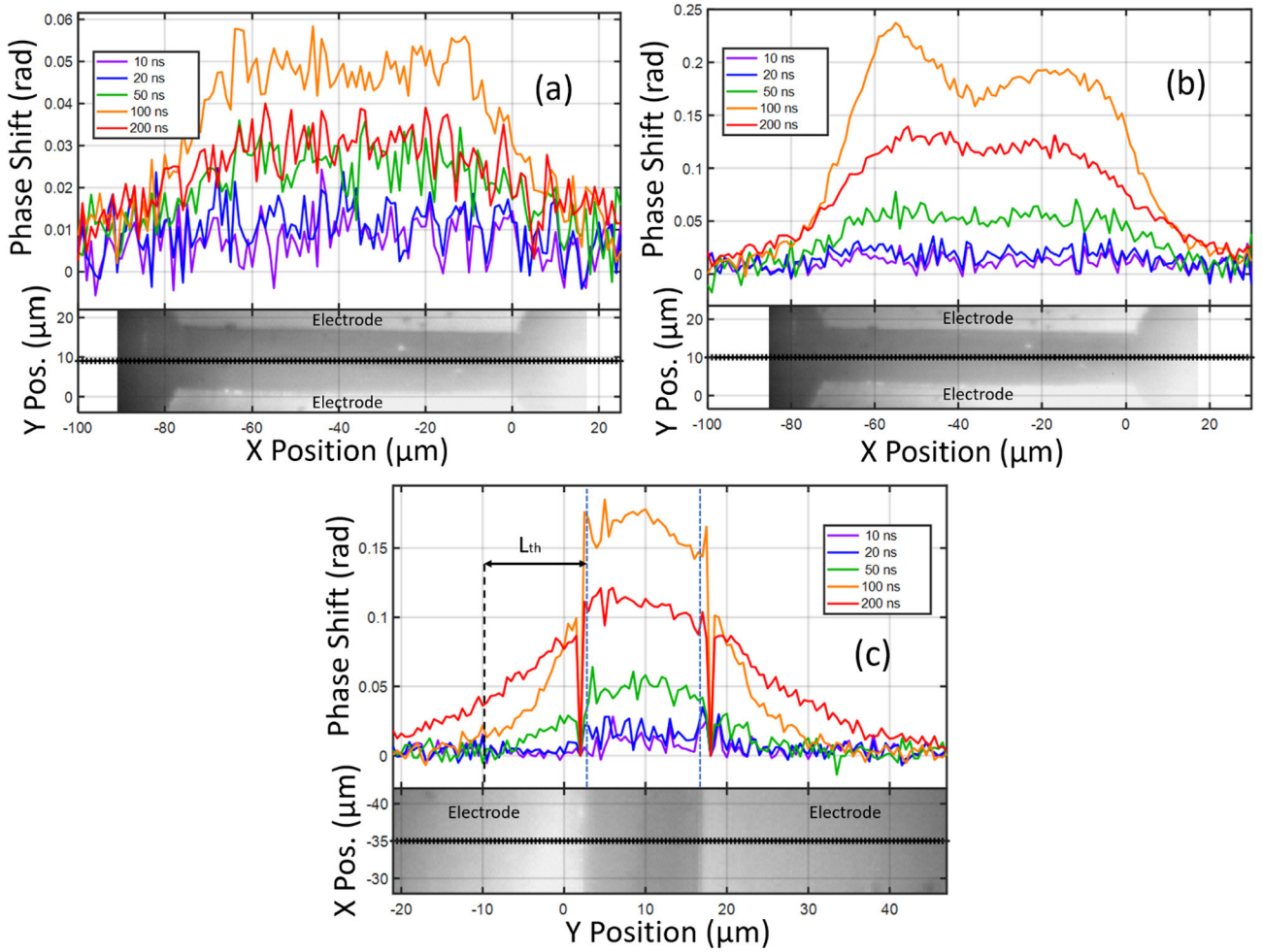


Fig. 3. Phase shift measurement on sample D ($[B] = 3.5 \times 10^{19} \text{ cm}^{-3}$) along a scanning line parallel to the electrodes for different times and a current of (a) 0.05 A and (b) 0.25 A. (c) is the evolution of the phase shift distribution along a scanning line perpendicular to the electrodes, in the center of the device, for currents of 0.25 A with a positive polarity on the right electrode. The photographs are backside infrared images of the device active area including the scanning direction (black bold line).

the electrodes edge (i.e. at $Y = 3$ and $Y = 17 \mu\text{m}$) are optical artefacts. Unfortunately, they are at the positions where the phase shift distribution has the largest gradient and therefore prohibit establishing its exact shape.

The spreading of phase shift with time and its apparent increase after the end of the pulse outside the spatial limits of the inter-electrode gap are due to thermal diffusion. The diffusion length in Fig. 3c is estimated as the distance from the edge of the electrode for which the temperature decreases by around 90% and it is consistent with the diamond diffusion length ($L_{th} = 11 \mu\text{m}$ for $t = 100 \text{ ns}$) as estimated from

$$L_{th} = \sqrt{\frac{k_T t}{c_V}}, \quad (1)$$

with the thermal conductivity ($k_T = 22 \text{ W.cm}^{-1}.\text{K}^{-1}$) (reference [23]), the volumetric heat capacity ($c_V = 1.83 \text{ J.cm}^{-3}.\text{K}^{-1}$) and the time (t).

4. Modeling

The I-V characteristics, and voltage/current transient waveforms were modeled by the finite element method (Atlas by Silvaco) using the drift diffusion and thermo-dynamic approach (i.e. drift diffusion model with thermal equation) based on the dependences of transport parameters and hole concentration on the electric field and the temperature. The concentric electrodes with their cylindrical geometry simplify the

simulations to a two-dimensional problem in space. A substrate depth of $100 \mu\text{m}$ has been considered. A 50 Ohm resistor has been used between the simulated device and voltage source to emulate the 50 Ohm internal resistance of the transmission-line pulse generator's equivalent circuit. The simulated area is a rectangle with a height of $150 \mu\text{m}$ and a width of $100 \mu\text{m}$ with two Ohmic contacts on top of it. The mesh size was set to $0.1 \mu\text{m}$ between the electrodes and in the doped diamond layer and progressively set to $5 \mu\text{m}$ at the limit of the simulated area. The default values of tolerance from the Atlas software (Silvaco) [24] were used for the simulations (see Table A in the Appendix section).

As the super-linearity is observed at voltages for which no significant heating is expected, additional mechanisms have to be considered to explain this behavior: Phonon-Assisted Tunneling Effect (PATE), Poole-Frenkel Effect (PFE) [15,16], and Impurity Impact Ionization (III) [11,25]. The simulation parameters used for each model are reported in Table 1.

Hole mobility μ_h and activation energy E_a dispersion with temperature and dopant concentration are crucial parameters in modeling the current and voltage in simulated devices. The temperature and impurity concentration dependence of the hole mobility was modeled using the equations derived by S. Kagamihara et al. [26] from the work of D. M. Caughey and R. E. Thomas [27] (see Eqs. (2) to (5)):

$$\mu_{h0}(T, N_{imp}) = \mu_h(T_{amb}, N_{imp}) \left(\frac{T}{300} \right)^{-\beta(N_{imp})}, \quad (2)$$

Table 2
Fitting parameters for the mobility model taken from [28].

μ^{\min} (cm ² .V ⁻¹ .s ⁻¹)	0
μ^{\max} (cm ² .V ⁻¹ .s ⁻¹)	2016
γ_{μ}	0.73
N_{μ} (cm ⁻³)	3.25×10^{17}
β^{\min}	0
β^{\max}	3.11
γ_{β}	0.617
N_{β} (cm ⁻³)	4.1×10^{18}

$$\mu_{h0}(T_{amb}, N_{imp}) = \mu^{\min} + \frac{\mu^{\max} - \mu^{\min}}{1 + \left(\frac{N_{imp}}{N_{\mu}}\right)^{\gamma_{\mu}}}, \quad (3)$$

$$\beta(N_{imp}) = \beta^{\min} + \frac{\beta^{\max} - \beta^{\min}}{1 + \left(\frac{N_{imp}}{N_{\beta}}\right)^{\gamma_{\beta}}}, \quad (4)$$

$$N_{imp} = N_A + N_D, \quad (5)$$

where N_A and N_D are the acceptor and the donor concentrations, respectively and $T_{amb} = 300$ K. The β^{\min} , β^{\max} , γ_{β} , N_{β} , μ^{\min} , μ^{\max} , γ_{μ} and N_{μ} parameters based on reference [28] are reported in Table 2.

The dependence of the mobility on the electric field E and the saturation velocity v_{sat} is given in (see reference [27])

$$\mu_h(E, T, N_{imp}) = \mu_{h0}(T, N_{imp}) \left(\frac{1}{1 + \left(\frac{\mu_{h0}(T, N_{imp})E}{v_{sat}}\right)^{\beta_{sat}}} \right)^{\frac{1}{\beta_{sat}}}. \quad (6)$$

The drift velocity for holes is then given by:

$$v_d(E, T, N_{imp}) = \mu_h(E, T, N_{imp})E. \quad (7)$$

v_{sat} and β_{sat} were obtained by fitting the hole-drift velocity data from reference [29] measured on (100) diamond samples at 300 K using Eqs. (6) and (7). The resulting fitting is given in Fig. 4.

The activation energy E_a of boron acceptors decreases with increasing doping concentration due to the interaction between carriers and ionized impurities [30]. In this work, we used a modified Pearson and Bardeen [31] model, see Eq. (8), which fits the experimental data better:

$$E_a(N_A) = E_I - aN_A^b, \quad (8)$$

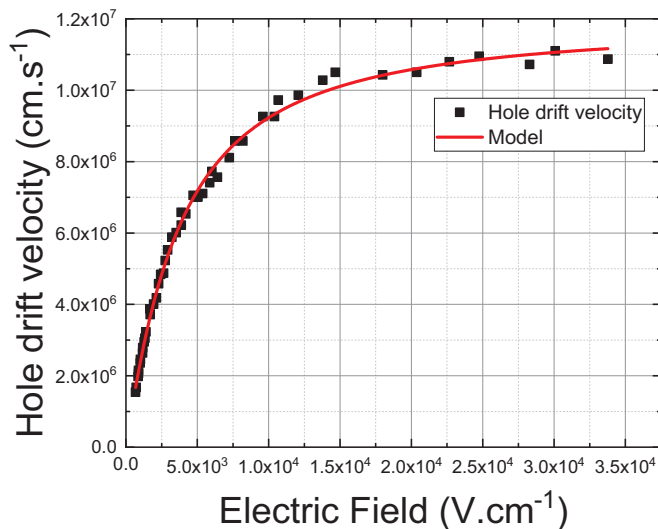


Fig. 4. Experimental [29] and calculated hole drift velocity as a function of the electric field.

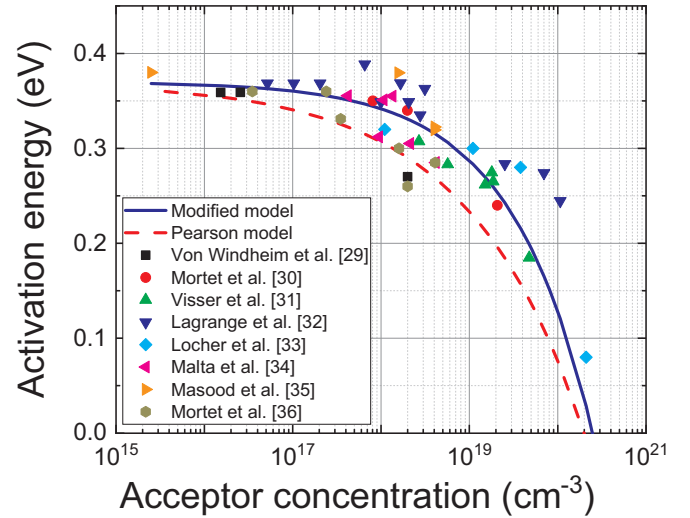


Fig. 5. Dispersion of activation energy with boron concentration.

with $E_I = 0.37$ eV. The coefficients a (1.2×10^{-10} eV.cm^{3/2.15}) and b (1/2.15) were determined by fitting experimental values from the literature [32–39] using the least square method. In the original Pearson and Bardeen model, only a is used as a fitting parameter and $b = 1/3$. Fig. 5 shows that the modified model clearly offers a better fit of the experimental data compared to the original model and gives boron activation energy with a root mean square error of 7×10^{-3} eV.

PATE is a type of field emission due to the absorption of phonons by electrons or holes trapped at an impurity level. Thanks to the energy acquired from the phonon absorption and under the influence of an external electric field, the trapped carriers can tunnel through the energy barrier and reach the conduction or valence band. PATE is described by the equations presented in reference [40]. The comparison between experimental data and simulated I-V curves using PATE model is shown in Fig. 6 (black dashed lines). The simulated I-V characteristics do not match the experimental data. The exponential behavior is not observed and the simulated I-V curve barely deviates from a classic linear Ohmic model. PATE alone cannot explain the behavior of the I-V characteristics of the studied boron-doped diamond samples.

Besides PATE, PFE might also contribute to non-linear I-V characteristics. In PFE, the energy barrier of a charged acceptor (or donor) energy level and the valence (or conduction) band decreases because of the dissymmetry in the impurity potential well in the external electric field and facilitates carrier emission by PATE. PFE has been previously reported in undoped diamond [15]. Since the boron impurities in diamond are, for the most part, not ionized at room temperature, PFE should not have a large influence on the I-V characteristics.

The modeled I-V characteristics, including PFE and PATE, are reported in Fig. 6 (red dashed lines). PFE has been included in the simulation using the model embedded in the finite element simulator Atlas (Silvaco). These new simulated I-V characteristics are nearly identical to the one including PATE only and they show that PFE and PATE have a limited influence on the non-linear I-V characteristic of boron-doped diamond at high electric field. This result is also consistent with the study of A.K. Jonscher [41], which shows the negligible contribution of PFE effect in electrical conductivity in crystalline semiconductors.

To determine the impact of III on the electrical properties of boron-doped diamond, we followed the same approach as in reference [25] using the classical band-to-band impact ionization equations to model the current multiplication from the boron acceptor.

In this case, the current multiplication coefficient is given by

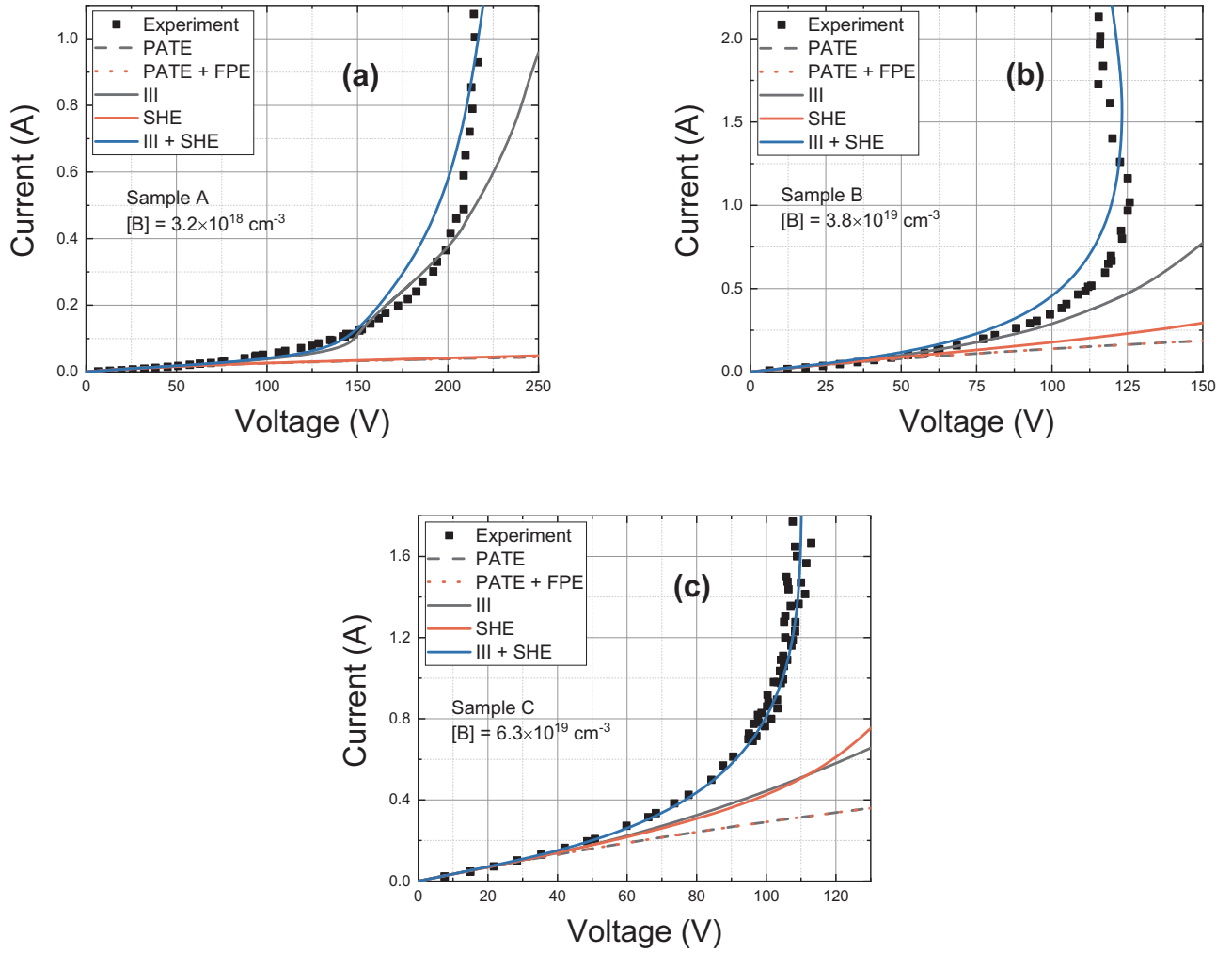


Fig. 6. Experimental (symbols) and simulated (lines and dashed lines) pulsed I-V characteristics using a combination of PATE, PFE, III, and SHE ($t = 100$ ns) for (a) sample A, (b) B, and (c) C. (For interpretation of the references to color in this figure, the reader is referred to the web version of this article.)

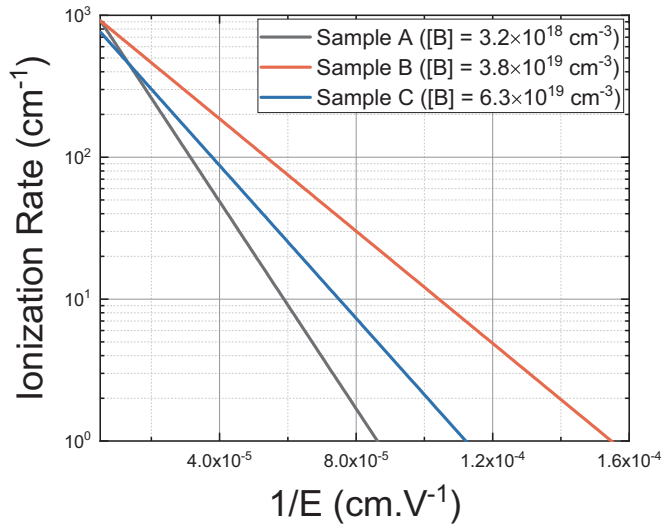


Fig. 7. Ionization rate α as a function of the reciprocal electric field.

$$M = \frac{1}{1 - \int_0^L \alpha_p \exp[-\int_0^x dx'(\alpha_p - \alpha_n)] dx'} \quad (9)$$

where L is the distance between the electrodes and α_p and α_n are the

ionization rate for holes and electrons respectively. We assume $\alpha_p = \alpha_n = \alpha$ [42] for simplification. The ionization rate α , which reflects the number of ionization events per unit of length is given by (see reference [43])

$$\alpha(E) = A_\alpha \exp(-B_\alpha/E), \quad (10)$$

where $E = U/L$ is the electric field, U is the voltage difference between the two electrodes, and A and B are fitting parameters. This simplification leads to a new expression of the current multiplication coefficient given in

$$M = \frac{1}{1 - L\alpha(U)}. \quad (11)$$

This model does not take into account the temperature dependence of the ionization rate observed in Si and Ge [44]. However, L. Tirino et al. [45] studied the influence of temperature for various wide band gap semiconductors and reached the conclusion that the temperature dependence of the ionization rate is mainly due to the temperature dependence of the phonon scattering rates. He also found out that the higher the optical phonon energy is, the less sensitive to temperature the impact ionization coefficients will be. For example, 3C-SiC has an optical phonon energy of 120 meV and its ionization rate was found to be almost insensible to temperature variations from 300 to 500 K. As a comparison, J. Pernot et al. [46] calculated an optical phonon energy of 165 meV for diamond from the data reported in [47]. Therefore, the ionization rate in diamond should be independent of temperature.

Ionization rates were determined by fitting the I-V curves using Eqs. (6), (10), and (11) in the region of negligible SHE, i.e. without temperature variation during the pulses (e.g. between 0 and 100 V for sample B). To simplify the calculation, the electric field is assumed to be constant between the electrodes, i.e. the edge effects due to the electrodes are neglected. Fig. 7 shows the determined ionization rate as a function of the inverse electric field for boron-doped diamond samples A, B, and C. Although there is no clear variation with boron concentration, the variation of the determined ionization rate is consistent for all boron concentrations, i.e. it increases and saturates at values of ca. 10^3 cm^{-1} for voltages (electric fields) superior to 100 V (70 kV.cm^{-1}).

The finite element simulated currents due to the III effect using determined ionization rates are compared to the experimental I-V curves in Fig. 6 (black lines). They reproduce correctly the exponential behavior of the current at low voltage, but are unable to reproduce its steep increase at high voltage, which is attributed to thermal runaway as indicated by TIM measurements.

To model the SHE, we used temperature dependent thermal conductivity (see reference [24]) and volumetric heat capacity given respectively by

$$k_T(T) = k_T(300 \text{ K}) \left(\frac{T}{300} \right)^{-m}, \quad (12)$$

with $m = 1$, and

$$c_V(T) = A_{c_V} + B_{c_V} T + C_{c_V} T^2 + \frac{D_{c_V}}{T^2}. \quad (13)$$

The parameters A_{c_V} , B_{c_V} , C_{c_V} , and D_{c_V} were determined by fitting the experimental values of volumetric heat capacity as a function of the temperature from reference [48]. The heat generation H term is given by

$$H = (\vec{J}_n + \vec{J}_p) \cdot \vec{E}, \quad (14)$$

where J_n and J_p are respectively the electron (negligible) and hole current density and E is the electric field. The concentration of donors is adjusted so that the simulated and experimental I-V curves have the same resistance between electrodes at low voltage. The resulting simulated I-V curves using a combination of III and SHE satisfactorily model the experimental non-linear current increase and the NDR for all samples as shown on Fig. 6 (blue lines).

In order to confirm the significant role of the III effect, I-V characteristics have been modeled using only SHE (see the red lines in Fig. 6), i.e. without the III effect. Although the simulated characteristic fits correctly the initial linear part, the current increases at a lower rate compared to the experimental I-V characteristic. This result shows that

SHE is not accountable alone for the observed I-V characteristic, even though it has a predominant effect at high electric field.

Fig. 8a shows the evolution of the simulated hole concentration at $t = 100 \text{ ns}$ as a function of voltage for samples A, B and C. The hole concentration exhibits super linear behavior, which is consistent with the I-V characteristics shown in Fig. 6. Sample A shows a slowdown of the hole multiplication above 165 V, which can be attributed to saturation of the carrier velocity described in Eq. (6). Fig. 8b shows the corresponding evolution of the maximum temperature as a function of the dissipated power. The temperature increases proportionally with the dissipated power for sample B and C. The temperature evolution in sample A on the other hand has a sub-linear behavior. The difference might be explained by the more dominant impact of saturation velocity in sample A due to the higher mobility of holes in this sample.

As mentioned previously, the empirical model presented by S. Kagamihara et al. [26] was used to calculate the hole mobility. The main condition for this model to be applicable is that the evolution of the mobility should be dominated by phonon scattering. In order to make sure this is true in the case of this study, the temperature and hole concentration from Fig. 8a and b were used to calculate the relaxation time, i.e. the time between to scattering events, for neutral impurity scattering, ionized impurity scattering, acoustic phonon scattering, and optical phonon scattering. The calculation was done for both the minimum and maximum power (i.e. the first and last point) of each simulated curve in Fig. 8a and b. The formulas used for the calculation are presented in the work of J. Pernot et al. [46], and D. M. Caughey and R. E. Thomas [27]. The results are presented in Table 3. The phonon scattering events have a relaxation time which is about four orders of magnitude smaller than the ones of neutral and ionized impurities for minimum and maximum power. It means that the evolution of the mobility is largely dominated by phonon scattering at low applied power but also for high power despite the increase in the number of ionized impurities due to III and SHE. It also confirms the validity of the mobility model used for the simulation.

Fig. 9a and b show respectively the simulated voltage and current waveforms for sample B with V_{ch} as the varying parameter. Fig. 9c shows the corresponding evolution of the maximal temperature. For device voltages less than 110 V (i.e. $V_{ch} < 125 \text{ V}$), the voltage waveform is nearly flat over time, which is consistent with the assumption used for the calculation of the ionization rate α , that the temperature has little influence on the shape of the I-V characteristic at low voltage. However, for higher initial device voltage (i.e. $V_{ch} > 125 \text{ V}$), the voltage is decreasing with time, due to thermal ionization of boron acceptor impurities, which decreases the resistivity of the sample during the pulse. For pulses with a starting voltage value over 200 V, the voltage value at the end of the pulse decreases when the starting

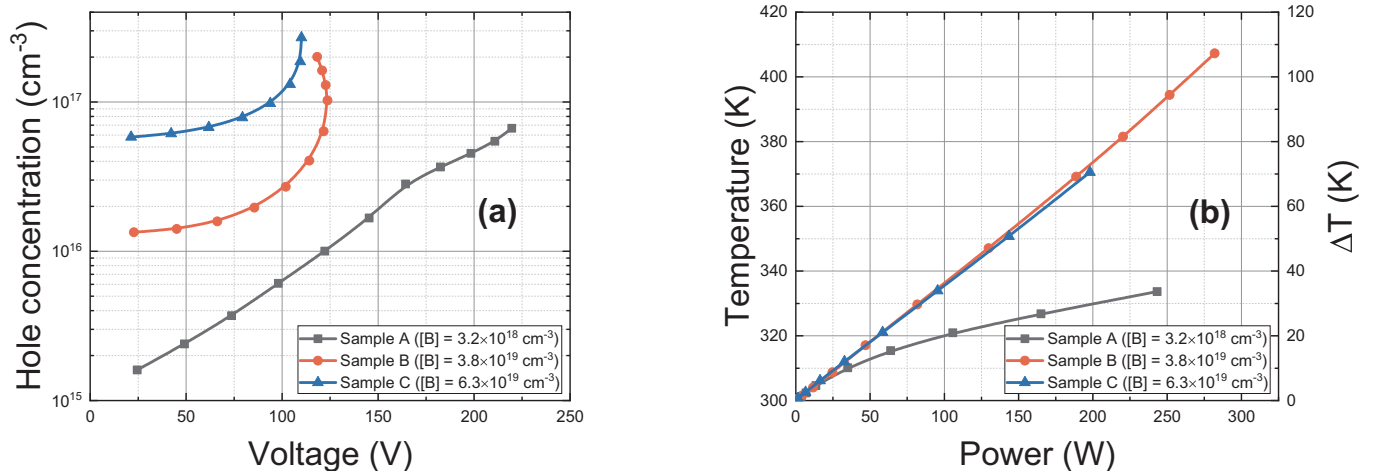


Fig. 8. Simulated hole concentration as a function of voltage (a) and maximum temperature as a function of power (b) in samples A, B and C.

Table 3

Relaxation times calculated for neutral impurity scattering (τ_{NI}), ionized impurity scattering (τ_{II}), acoustic phonon scattering (τ_{AC}), and optical phonon scattering (τ_{OP}) for samples A, B, and C for minimum and maximum applied power.

	Sample A	Sample B	Sample C
Relaxation times (minimum power)			
Neutral impurity τ_{NI} (s)	4.4×10^{-7}	3.9×10^{-8}	2.4×10^{-8}
Ionized impurity τ_{II} (s)	8.4×10^{-8}	2.3×10^{-9}	1.1×10^{-9}
Acoustic phonon τ_{AC} (s)	5.2×10^{-12}	5.2×10^{-12}	5.2×10^{-12}
Optical phonon τ_{OP} (s)	1.5×10^{-12}	1.5×10^{-12}	1.5×10^{-12}
Relaxation times (maximum power)			
Neutral impurity τ_{NI} (s)	4.6×10^{-7}	4.1×10^{-8}	2.4×10^{-8}
Ionized impurity τ_{II} (s)	6.0×10^{-8}	3.4×10^{-9}	1.4×10^{-9}
Acoustic phonon τ_{AC} (s)	4.5×10^{-13}	3.3×10^{-13}	3.8×10^{-13}
Optical phonon τ_{OP} (s)	7.5×10^{-13}	2.5×10^{-13}	4.1×10^{-13}

voltage increases. On the other hand, in Fig. 9b, the value of the current at the end of the pulse increases steadily when the loading DC voltage increases. The combination of the decrease of the instantaneous voltage and increase of the instantaneous current is responsible for the appearance of the NDR regime in sample B for high loading DC voltage visible in Fig. 6b. A similar behavior is observable in experimental waveforms measured on sample B in Fig. 1 and it is attributed to SHE, which causes an increase in temperature with time and with V_{ch} ,

evidenced by TIM measurements in Fig. 3 and confirmed by simulation in Fig. 9c for sample B. The simulation shows that temperature reaches a maximum value of 407 K for $V_{ch} = 237.5$ V.

Fig. 10a shows the simulated temperature distribution for sample D under conditions similar to the ones used for TIM measurements in Fig. 3c (i.e. for a current of 0.25 A) at $t = 100$ ns for two different depths: black squares represent the surface temperature distribution and the red dots the temperature for a distance of 10 μm from the surface. The vertical dashed lines represent the limits of the electrodes. Due to the stripe layout of samples used for TIM, in this case, the simulation was performed in 2D rectangular geometry which is still a good approach for the use of short pulses. One can observe that the surface temperature peaks at the right electrode edge (the ground electrode) with maximum value of about 440 K. The temperature distribution in the depth is smeared. The phase shift distribution from the 2D temperature profile was also calculated using equations in reference [18] and taking into account diamond thermo-optical coefficient from the work of V. Y. Yurov et al. [49]. In brief, the phase shift is the integral of temperature along the laser beam path weighted by the thermo-optical coefficient [18,19]. The phase shift distribution at $t = 100$ ns is plotted in Fig. 10b. The peak phase shift value near 0.14 rad is within the experimental error to the experiment in Fig. 3c. The calculated phase shift maximum in Fig. 10b is also shifted toward the right electrode but is smeared due to significant temperature contribution from the bulk. This shift in the phase shift distribution is however not distinguishable in experiment in Fig. 3c which can be

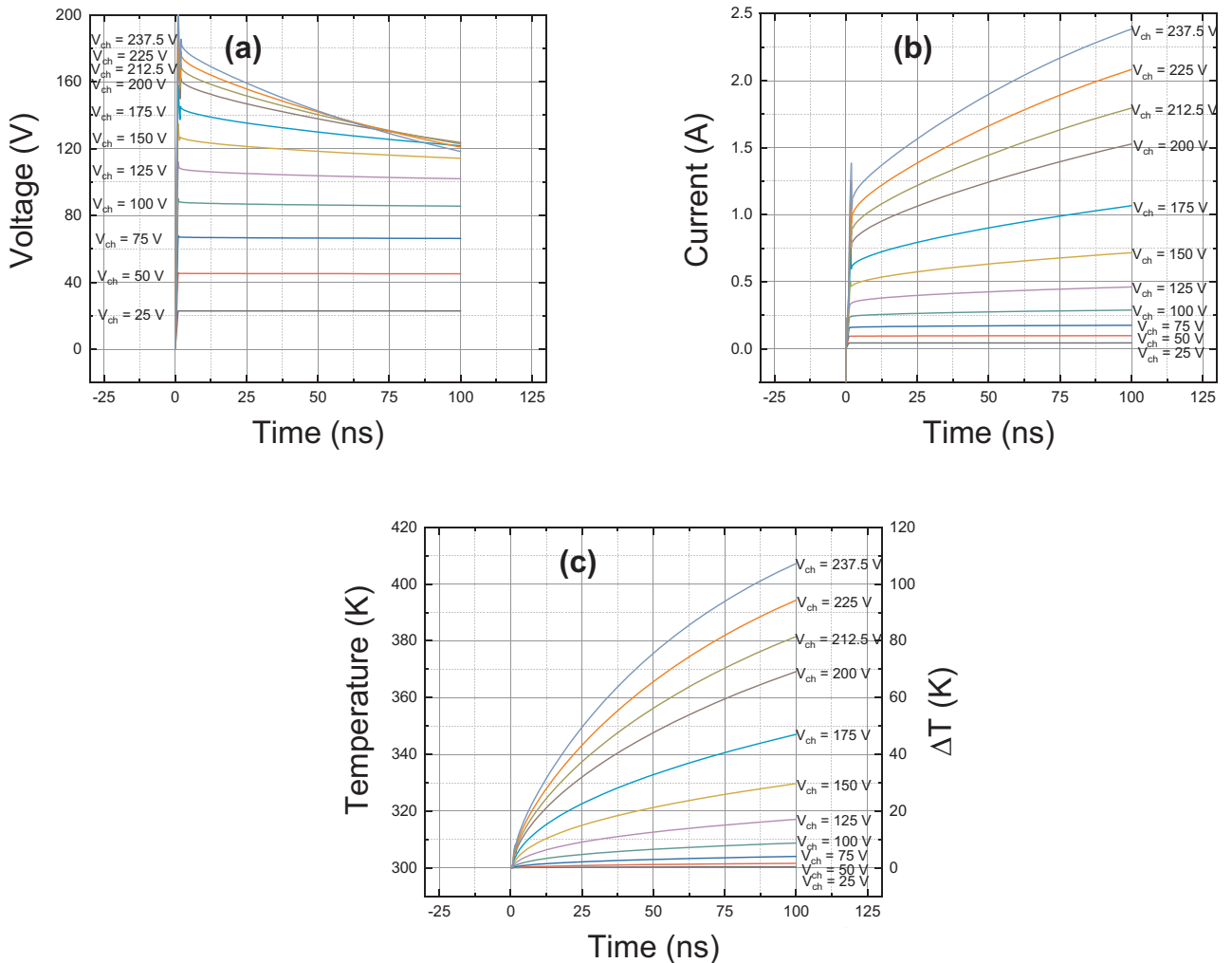


Fig. 9. Simulated voltage (a), current (b) waveforms, and maximum temperature (c) in sample B for an increasing amplitude of V_{ch} .

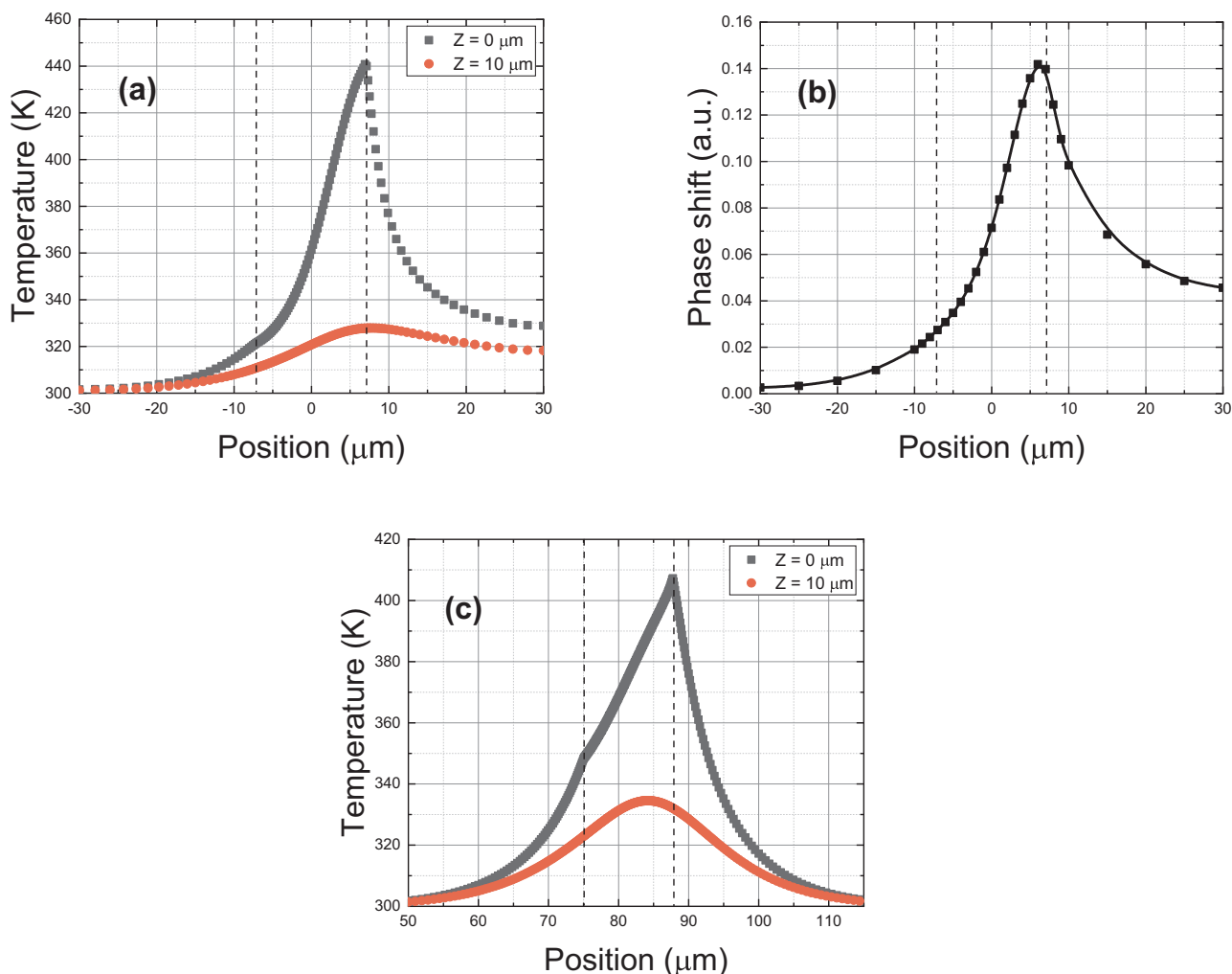


Fig. 10. Simulated temperature (a) and phase shift (b) distribution along a scanning line perpendicular to the electrodes for sample D at a current of 0.25 A and temperature distribution for sample B at a current of 2.4 A ($V_{ch} = 237.5$ V) (c). The temperature is given at the surface of the sample ($Z = 0 \mu\text{m}$) and for a depth of $10 \mu\text{m}$ in the diamond ($Z = 10 \mu\text{m}$). The time instant is $t = 100$ ns.

attributed to experimental uncertainty [18] and/or model imperfection. Fig. 10c shows the simulated temperature distribution for sample B (electrodes with cylindrical geometry) for a current of 2.4 A (i.e. $V_{ch} = 237.5$ V) and give similar results to what was observed with sample D. The surface temperature peaks at the positive electrode with a maximum value of 407 K. This maximum is consistent with the temperature value for the same condition at the pulse end (see top curve in Fig. 9c). The temperature distribution in the depth is smeared and the peak is shifted toward the middle of the inter-electrode gap.

The relatively good quantitative agreement between our experiments and simulations indicates that our model describes the transport quite satisfactorily. It means that hot carrier effects [50–53], like possible difference between the hot hole and lattice temperature does not need to be included explicitly. In particular, the carrier thermalization (energy relaxation) time constant in diamond is in the order of tens of ps [53], which is much shorter than the time scale of 10–100 ns considered in this study. The hot carrier effects are, however, included implicitly in our model since impurity impact ionization and velocity saturation are in fact due to hot carriers.

5. Conclusions

The experimental exponential behavior at low current/field and steep super-exponential (with NDR) behavior at high current/field of I-V characteristics measured on boron doped diamond devices were

satisfactorily modeled by finite element simulation. The exponential I-V behavior is attributed to III as previously suggested in reference [11], whereas the high currents at high electric fields can only be explained by including SHE. The short linear part of the curve for very low voltages can be attributed to simple Ohmic behavior as the electric field is not high enough to produce III. The role of SHE is supported by TIM measurements, which show a thermal runaway effect at the onset of NDR, which is consistent with simulations. In summary, the high electric field I-V characteristics of boron-doped diamond are the result of the III effect and its combination with SHE.

Author statement

N. Lambert: Writing - Original Draft, Methodology, Investigation, Data Curation, Visualization.

A. Taylor: Resources, Visualization.

P. Hubík: Resources.

J. Bulíř: Resources.

J. More-Chevalier: Resources.

H. Karaca: Investigation, Formal analysis.

C. Fleury: Investigation, Formal analysis.

J. Voves: Resources.

Z. Šobáň: Resources.

D. Pogany: Writing - Review & Editing, Resources, Methodology.

V. Mortet: Writing - Review & Editing, Conceptualization,

Supervision.

Declaration of competing interest

The authors declare that they have no known competing financial interests or personal relationships that could have appeared to influence the work reported in this paper.

Appendix A

Table A

Default values of tolerances used in the Silvaco Atlas finite element simulation [24].

PX.TOL	Relative tolerance for the potential equation	10^{-5}
PR.TOL	Absolute tolerance for the Poisson equation	10^{-26}
CX.TOL	Relative tolerance for the continuity equation	10^{-5}
CR.TOL	Absolute tolerance for the continuity equation	5×10^{-18}
TCX.TOL	Relative tolerance for convergence of the carrier temperature equations	10^{-5}
TLX.TOL	Relative tolerance for convergence of the lattice temperature equation	10^{-5}
TCR.TOL	Absolute tolerance for convergence of the carrier temperature equations	100
TLR.TOL	Absolute tolerance for convergence of the lattice temperature equation	100
IX.TOL	Relative current convergence criteria	5×10^{-4}
IR.TOL	Absolute current convergence criteria	5×10^{-11}

References

- [1] Semiconductor diamond, Ultra-wide Bandgap Semicond, Elsevier, Mater, 2019, pp. 111–261, <https://doi.org/10.1016/B978-0-12-815468-7.00002-0>.
- [2] M.-A. Pinault-Thaury, S. Temgoua, R. Gillet, H. Bensalah, I. Stenger, F. Jomard, R. Issaoui, J. Barjon, Phosphorus-doped (113) CVD diamond: a breakthrough towards bipolar diamond devices, Appl. Phys. Lett. 114 (2019) 112106, <https://doi.org/10.1063/1.5079924>.
- [3] A. Lazea, Y. Garino, T. Teraji, S. Koizumi, High quality p-type chemical vapor deposited (111)-oriented diamonds: growth and fabrication of related electrical devices, Phys. Status Solidi A 209 (2012) 1978–1981, <https://doi.org/10.1002/pssa.201228162>.
- [4] A.F. Sartori, M. Fischer, S. Gsell, M. Schreck, *In situ* boron doping during heteroepitaxial growth of diamond on Ir/YSZ/Si, Phys. Status Solidi A 209 (2012) 1643–1650, <https://doi.org/10.1002/pssa.201200221>.
- [5] H. Umezawa, S. Shikata, T. Funaki, Diamond Schottky barrier diode for high-temperature, high-power, and fast switching applications, Jpn. J. Appl. Phys. 53 (2014), <https://doi.org/10.7567/JJAP.53.05FP06> 05FP06.
- [6] P.-N. Volpe, P. Muret, J. Pernot, F. Omnès, T. Teraji, F. Jomard, D. Planson, P. Brosselard, N. Dheilil, B. Vergne, S. Scharnholtz, High breakdown voltage Schottky diodes synthesized on p-type CVD diamond layer, Phys. Status Solidi A 207 (2010) 2088–2092, <https://doi.org/10.1002/pssa.201000055>.
- [7] J. Wang, D. Zhao, W. Wang, X. Zhang, Y. Wang, X. Chang, Z. Liu, J. Fu, K. Wang, H.-X. Wang, Diamond Schottky barrier diodes with floating metal rings for high breakdown voltage, Mater. Sci. Semicond. Process. 97 (2019) 101–105, <https://doi.org/10.1016/j.mssp.2019.03.004>.
- [8] T. Matsumoto, H. Kato, K. Oyama, T. Makino, M. Ogura, D. Takeuchi, T. Inokuma, N. Tokuda, S. Yamasaki, Inversion channel diamond metal-oxide-semiconductor field-effect transistor with normally off characteristics, Sci. Rep. 6 (2016), <https://doi.org/10.1038/srep31585>.
- [9] Z. Ren, W. Chen, J. Zhang, J. Zhang, C. Zhang, G. Yuan, K. Su, Z. Lin, Y. Hao, High performance single crystalline diamond normally-off field effect transistors, IEEE J. Electron Devices Soc. 7 (2019) 82–87, <https://doi.org/10.1109/JEDS.2018.2880005>.
- [10] V. Mortet, D. Trémouilles, J. Bulfř, P. Hubík, L. Heller, E. Bedel-Pereira, A. Soltani, Peculiarities of high electric field conduction in p-type diamond, Appl. Phys. Lett. 108 (2016) 152106, <https://doi.org/10.1063/1.4946853>.
- [11] V. Mortet, A. Soltani, Impurity impact ionization avalanche in p-type diamond, Appl. Phys. Lett. 99 (2011) 202105, <https://doi.org/10.1063/1.3662403>.
- [12] V. Mortet, L. Drbohlavova, N. Lambert, A. Taylor, P. Ashcheulov, M. Davydova, J. Lorincik, M. Aleshin, P. Hubík, Conductivity of boron-doped diamond at high electrical field, Diam. Relat. Mater. 98 (2019) 107476, <https://doi.org/10.1016/j.diamond.2019.107476>.
- [13] K.D. Morhard, R.P. Huebener, W. Clauss, J. Peinke, Low-temperature avalanche breakdown in p-Ge: influence of the acceptor concentration, J. Appl. Phys. 71 (1992) 3336–3338, <https://doi.org/10.1063/1.350955>.
- [14] V.I. Sankin, A.M. Monakhov, P.P. Shkrebiy, P.L. Abramov, N.I. Sablina, N.S. Averkiev, Peculiarities of impact ionization of Impurity Al in SiC polytypes, Appl. Phys. Lett. 97 (2010) 262118, <https://doi.org/10.1063/1.3527964>.
- [15] M. Girolami, A. Bellucci, P. Calvani, R. Flammini, D.M. Trucchi, Radiation-assisted Frenkel-Poole transport in single-crystal diamond, Appl. Phys. Lett. 103 (2013) 083502, <https://doi.org/10.1063/1.4818904>.
- [16] G. Vincent, A. Chantre, D. Bois, Electric field effect on the thermal emission of traps in semiconductor junctions, J. Appl. Phys. 50 (1979) 5484, <https://doi.org/10.1063/1.326601>.
- [17] M. Davydova, A. Taylor, P. Hubík, L. Fekete, L. Klimša, D. Trémouilles, A. Soltani, V. Mortet, Characteristics of zirconium and niobium contacts on boron-doped diamond, Diam. Relat. Mater. 83 (2018) 184–189, <https://doi.org/10.1016/j.diamond.2018.02.009>.
- [18] D. Pogany, S. Bychikhin, C. Furbock, M. Litzberger, E. Gornik, G. Groos, K. Esmark, M. Stecher, Quantitative internal thermal energy mapping of semiconductor devices under short current stress using backside laser interferometry, IEEE Trans. Electron Devices 49 (2002) 2070–2079, <https://doi.org/10.1109/TED.2002.804724>.
- [19] M. Litzberger, C. Furbock, S. Bychikhin, D. Pogany, E. Gornik, Scanning heterodyne interferometer setup for the time-resolved thermal and free-carrier mapping in semiconductor devices, IEEE Trans. Instrum. Meas. 54 (2005) 2438–2445, <https://doi.org/10.1109/TIM.2005.858121>.
- [20] Y. Song, B.D. Peng, G.Z. Song, Z.Q. Yue, B.K. Li, J.M. Ma, L. Sheng, B.J. Duan, H.X. Wang, Investigating non-equilibrium carrier lifetimes in nitrogen-doped and boron-doped single crystal HPHT diamonds with an optical method, Appl. Phys. Lett. 112 (2018) 022103, <https://doi.org/10.1063/1.5019587>.
- [21] T. Shimomura, Y. Kubo, J. Barjon, N. Tokuda, I. Akimoto, N. Naka, Quantitative relevance of substitutional impurities to carrier dynamics in diamond, Phys. Rev. Mater. 2 (2018) 094601, <https://doi.org/10.1103/PhysRevMaterials.2.094601>.
- [22] V.A. Vashchenko, V.F. Sinkevitch, Physical Limitations of Semiconductor Devices, Springer, New York, 2008.
- [23] J.R. Olson, R.O. Pohl, J.W. Vandersande, A. Zoltan, T.R. Anthony, W.F. Banholzer, Thermal conductivity of diamond between 170 and 1200 K and the isotope effect, Phys. Rev. B 47 (1993) 14850–14856, <https://doi.org/10.1103/PhysRevB.47.14850>.
- [24] Atlas User's Manual, (2018).
- [25] A.W. Livingstone, J.W. Allen, Impact ionization of deep impurities in zinc selenide, J. Phys. C Solid State Phys. 6 (1973) 3491–3500, <https://doi.org/10.1088/0022-3719/6/23/023>.
- [26] S. Kagamihara, H. Matsuura, T. Hatakeyama, T. Watanabe, M. Kushibe, T. Shinohe, K. Arai, Parameters required to simulate electric characteristics of SiC devices for n-type 4H-SiC, J. Appl. Phys. 96 (2004) 5601–5606, <https://doi.org/10.1063/1.1798399>.
- [27] D.M. Caughey, R.E. Thomas, Carrier mobilities in silicon empirically related to doping and field, Proc. IEEE 55 (1967) 2192–2193, <https://doi.org/10.1109/PROC.1967.6123>.
- [28] P.-N. Volpe, J. Pernot, P. Muret, F. Omnès, High hole mobility in boron doped diamond for power device applications, Appl. Phys. Lett. 94 (2009) 092102, <https://doi.org/10.1063/1.3086397>.
- [29] L. Reggiani, S. Bosi, C. Canali, F. Nava, S.F. Kozlov, Hole-drift velocity in natural diamond, Phys. Rev. B 23 (1981) 3050–3057, <https://doi.org/10.1103/PhysRevB.23.3050>.
- [30] G.L. Pearson, J. Bardeen, Electrical properties of pure silicon and silicon alloys containing boron and phosphorus, Phys. Rev. 75 (1949) 865–883, <https://doi.org/10.1103/PhysRev.75.865>.
- [31] V. Mortet, N. Lambert, P. Hubík, A. Soltani, Model of carrier multiplication due to impurity impact ionization in boron-doped diamond, TANGER Ltd., Brno, Czech Republic, 2018, pp. 41–45.
- [32] J.A. Von Windheim, V. Venkatesan, D.M. Malta, K. Das, Electrical characterization of semiconducting diamond thin films and single crystals, J. Electron. Mater. 22 (1993) 391–398, <https://doi.org/10.1007/BF02661667>.
- [33] V. Mortet, M. Daenen, T. Teraji, A. Lazea, V. Vorlicek, J. D'Haen, K. Haenen, M. D'Oleslaeger, Characterization of boron doped diamond epilayers grown in a

- NIRIM type reactor, *Diam. Relat. Mater.* 17 (2008) 1330–1334, <https://doi.org/10.1016/j.diamond.2008.01.087>.
- [34] E.P. Visser, G.J. Bauhuis, G. Janssen, W. Vollenberg, J.P. van Enkevort, L.J. Giling, Electrical conduction in homoepitaxial, boron-doped diamond films, *J. Phys. Condens. Matter* 4 (1992) 7365–7376, <https://doi.org/10.1088/0953-8984/4/36/011>.
- [35] J.-P. Lagrange, A. Deneuve, E. Gheeraert, A large range of boron doping with low compensation ratio for homoepitaxial diamond films, *Carbon* 37 (1999) 807–810, [https://doi.org/10.1016/S0008-6223\(98\)00275-9](https://doi.org/10.1016/S0008-6223(98)00275-9).
- [36] R. Locher, J. Wagner, F. Fuchs, M. Maier, P. Gonon, P. Koidl, Optical and electrical characterization of boron-doped diamond films, *Diam. Relat. Mater.* 4 (1995) 678–683, [https://doi.org/10.1016/0925-9635\(94\)05297-2](https://doi.org/10.1016/0925-9635(94)05297-2).
- [37] D.M. Malta, J.A. von Windheim, H.A. Wijnands, B.A. Fox, Comparison of the electrical properties of simultaneously deposited homoepitaxial and polycrystalline diamond films, *J. Appl. Phys.* 77 (1995) 1536–1545, <https://doi.org/10.1063/1.358905>.
- [38] A. Masood, M. Aslam, M.A. Tamor, T.J. Potter, Synthesis and electrical characterization of boron-doped thin diamond films, *Appl. Phys. Lett.* 61 (1992) 1832–1834, <https://doi.org/10.1063/1.108389>.
- [39] V. Mortet, J. Pernot, F. Jomard, A. Soltani, Z. Remes, J. Barjon, J. D'Haen, K. Haenen, Properties of boron-doped epitaxial diamond layers grown on (110) oriented single crystal substrates, *Diam. Relat. Mater.* 53 (2015) 29–34, <https://doi.org/10.1016/j.diamond.2015.01.006>.
- [40] G.A.M. Hurkx, D.B.M. Klaassen, M.P.G. Knuvers, F.G. O'Hara, A new recombination model describing heavy-doping effects and low-temperature behaviour, *Int. Tech. Dig. Electron Devices Meet., IEEE*, Washington, DC, USA, 1989, pp. 307–310, <https://doi.org/10.1109/IEDM.1989.74285>.
- [41] A.K. Jonscher, Free-carrier Poole-Frenkel effect in crystalline solids, *J. Phys. C Solid State Phys.* 3 (1970) L159–L162, <https://doi.org/10.1088/0022-3719/3/8/029>.
- [42] A. Hiraiwa, H. Kawarada, Figure of merit of diamond power devices based on accurately estimated impact ionization processes, *J. Appl. Phys.* 114 (2013) 034506, <https://doi.org/10.1063/1.4816312>.
- [43] A.G. Chynoweth, Ionization rates for electrons and holes in silicon, *Phys. Rev.* 109 (1958) 1537–1540, <https://doi.org/10.1103/PhysRev.109.1537>.
- [44] C.R. Crowell, S.M. Sze, Temperature dependence of avalanche multiplication in semiconductors, *Appl. Phys. Lett.* 9 (1966) 242–244, <https://doi.org/10.1063/1.1754731>.
- [45] L. Tirino, M. Weber, K.F. Brennan, E. Bellotti, M. Goano, Temperature dependence of the impact ionization coefficients in GaAs, cubic SiC, and zinc-blende GaN, *J. Appl. Phys.* 94 (2003) 423–430, <https://doi.org/10.1063/1.1579129>.
- [46] J. Pernot, P.N. Volpe, F. Omnès, P. Muret, V. Mortet, K. Haenen, T. Teraji, Hall hole mobility in boron-doped homoepitaxial diamond, *Phys. Rev. B* 81 (2010), <https://doi.org/10.1103/PhysRevB.81.205203>.
- [47] S.A. Solin, A.K. Ramdas, Raman spectrum of diamond, *Phys. Rev. B* 1 (1970) 1687–1698, <https://doi.org/10.1103/PhysRevB.1.1687>.
- [48] A.C. Victor, Heat capacity of diamond at high temperatures, *J. Chem. Phys.* 36 (1962) 1903–1911, <https://doi.org/10.1063/1.1701288>.
- [49] V.Yu. Yurov, E.V. Bushuev, A.F. Popovich, A.P. Bolshakov, E.E. Ashkinazi, V.G. Ralchenko, Near-infrared refractive index of synthetic single crystal and polycrystalline diamonds at high temperatures, *J. Appl. Phys.* 122 (2017) 243106, <https://doi.org/10.1063/1.5008387>.
- [50] J.B. Khurgin, K.-T. Tsen, J.-J. Song, M.J. Cohen, J.W. Glesener (Eds.), Mitigating hot phonons in high power optoelectronic devices based on wide gap semiconductors, 2007, <https://doi.org/10.1117/12.705110> San Jose, CA. p. 64710Y.
- [51] J. Liberis, I. Matulioniene, A. Matulionis, M.C. Lemme, H. Kurz, M. Först, Hot-phonon temperature and lifetime in biased boron-implanted SiO₂/Si/SiO₂ channels, *Semicond. Sci. Technol.* 21 (2006) 803–807, <https://doi.org/10.1088/0268-1242/21/6/017>.
- [52] S. Barman, G.P. Srivastava, Quantitative estimate of phonon scattering rates in different forms of diamond, *Phys. Rev. B* 73 (2006) 073301, <https://doi.org/10.1103/PhysRevB.73.073301>.
- [53] M. Kozák, F. Trojánek, P. Malý, Hot-carrier transport in diamond controlled by femtosecond laser pulses, *New J. Phys.* 17 (2015) 053027, <https://doi.org/10.1088/1367-2630/17/5/053027>.